Chinese Chemical Letters 35 (2024) 109595

Contents lists available at ScienceDirect

Chinese Chemical Letters

journal homepage: www.elsevier.com/locate/cclet

# Grain-refining $Co_{0.85}Se$@CNT cathode catalyst with promoted $Li_2O_2$ growth kinetics for lithium-oxygen batteries

Ruonan Yang[a], Jiajia Li[a], Dongmei Zhang[a], Xiuqi Zhang[a], Xia Li[a], Han Yu[a], Zhanhu Guo[b], Chuanxin Hou[c,*], Gang Lian[a,*], Feng Dang[a,*]

[a] School of Materials Science & Engineering, State Key Laboratory of Crystal Materials, Shandong University, Ji'nan 250061, China
[b] Integrated Composites Lab, Department of Mechanical and Construction Engineering, Northumbria University, Newcastle Upon Tyne, NE1 8ST, United Kingdom
[c] School of Environmental and Material Engineering, Yantai University, Yantai 264005, China

ARTICLE INFO

*Article history:*
Received 7 December 2023
Revised 2 January 2024
Accepted 29 January 2024
Available online 6 February 2024

*Keywords:*
Lithium-oxygen batteries
$Co_{0.85}Se$@CNT
Cathode catalysts
Grain-refiner
DFT calculation

ABSTRACT

Highly active cathode catalysts for efficient formation/decomposition of $Li_2O_2$ are essential for the performance improvement of lithium-oxygen batteries (LOBs). In this study, a grain-refining $Co_{0.85}Se$ catalyst with a lattice spacing of 2.69 Å of (101) plane closely matching with the (100) plane (2.72 Å) of $Li_2O_2$ was applied for high-performance LOBs. Highly (101) plane exposed $Co_{0.85}Se$@CNT was synthesized by a simple one-pot hydrothermal method. The $Co_{0.85}Se$ with the lattice matching effect not only led to the efficient conversion and polarized growth of $Li_2O_2$, but also prevented the formation of byproducts. Density functional theory (DFT) calculations reveal that $Co_{0.85}Se$ (101) plane has the intrinsic catalytic ability to generate/decompose $Li_2O_2$ during ORR/OER process, due to its homogeneous electron distribution, suitable adsorption energy, and promoted $Li_2O_2$ growth kinetics. As a consequence, the (101) plane highly exposed $Co_{0.85}Se$@CNT-80 electrode exhibited remarkable cycle stability over 2400 h at 100 mA/g and 290 cycles at 500 mA/g, which is about 2 times longer than other electrodes.



Lithium oxygen batteries (LOBs) based on reversible reaction $O_2 + 2Li^+ + 2e^- \leftrightarrow Li_2O_2$ are considered as one of the most promising electrochemical energy storage systems due to their high theoretical energy density (3500 Wh/kg), low cost and environmental friendliness [1–6]. Meanwhile, several challenges including poor circularity, low round-trip efficiency and serious polarization caused by sluggish kinetics of oxygen reduction reaction (ORR) and oxygen evolution reaction (OER) need to be addressed before practical utilization [7–16]. Nevertheless, it is urgent to develop new bifunctional catalysts to improve OER and ORR kinetics. In order to improve the reaction rate, it is necessary to optimize the cathode catalyst, since cathode is the main place of electrochemical reaction [6,17-19].

The reversible formation and decomposition of discharge product $Li_2O_2$ on the cathode catalyst is closely related to the electrochemical performance of LOBs to a great extent. Most researchers postulated that the formation/decomposition process of $Li_2O_2$ undergoes through $LiO_2$ intermediate, which is a strong oxidant and can lead to the passivation of the cathode catalyst and decomposition of electrolyte [4,20-22]. Furthermore, the accumulation of side products during the ORR/OER process also leads to the deterioration and capacity fading of LOBs cell [21,23-26]. It is reported that searching for a grain-refining agent catalyst with the lattice matching effect to discharge products, which can accelerate the reaction kinetics of discharge product for a controlled morphology and designed composition is a facile strategy to enhance the electrochemical performance of LOBs [20,27-29]. The grain-refining agents can serve as a grain promoter for the nucleation, initial growth and decomposition of discharge product through controlling the reaction kinetics based on lattice matching of the crystal structure between catalyst and discharge product. However, only few cathode catalysts have the lattice matching nature with $Li_2O_2$ or $LiO_2$. For example, IrLi can serve as a template for crystal $LiO_2$ growth because of the low interfacial energy ($-0.36$ eV/Å$^2$) and good lattice matching between IrLi (111) plane and $LiO_2$ (111), allowing the strong oxidant $LiO_2$ to be generated and stabilized [30]. $CeO_2$ effectively reduces overpotential during ORR and OER due to well matched interplanar spacing of $CeO_2$ (200) facet (2.72 Å) and $Li_2O_2$ (100) facet (2.74 Å) [27]. Hexagonal $MoSe_2$ with the same space group (P 63/mmc) and similar *a*, *b*-lattice parameters (3.288 Å) with $Li_2O_2$

* Corresponding authors.
*E-mail addresses:* chuanxin210@ytu.edu.cn (C. Hou), liangang@sdu.edu.cn (G. Lian), dangfeng@sdu.edu.cn (F. Dang).

https://doi.org/10.1016/j.cclet.2024.109595
1001-8417/

can act as the grain promoter to induce initial nucleation and epitaxial growth of $Li_2O_2$ grains [20]. The similar *d*-spacing of $Fe_2O_3$ (104) and $Li_2O_2$ (100) plane induces epitaxial growth of $Li_2O_2$ on the $Fe_2O_3$ surface which enhances the nucleation of $Li_2O_2$ and suppresses the formation of amorphous $Li_2O_2$ [28]. Interestingly, (101) plane of $Co_{0.85}Se$ exhibits the lattice plane *d*-spacing closing to that of $Li_2O_2$ (100) and is expected to act as an effective grain refiner for the formation/decomposition of discharge products. In addition, as a promising transition metal selenide, $Co_{0.85}Se$ figures a vacancy defect structure and special electronic structure, which has been already applied in water splitting [31] and sodium-ion batteries [32].

In this work, $Co_{0.85}Se$@CNT was applied as a grain-refining catalyst to investigate the lattice matching effect on the electrochemical performance of LOBs. The (101) plane highly exposed $Co_{0.85}Se$ nanocrystals with a size of 5–10 nm uniformly embedded on the CNT substrate. The (101) plane of $Co_{0.85}Se$ with a lattice spacing of 2.69 Å is closely matches with the (100) plane (2.72 Å) of $Li_2O_2$, which is favor to the conversion from $LiO_2$ to $Li_2O_2$ and the epitaxial growth of $Li_2O_2$ crystal, reduce the overpotentials and extend the cycle life. It is identified that the (101) plane highly exposed $Co_{0.85}Se$@CNT cathode exhibited low overpotentials and superior electrochemical performance. The effect of epitaxial growth of discharge product under the existence of $Co_{0.85}Se$ nanocrystals was observed. Density functional theory (DFT) calculations demonstrated that $Co_{0.85}Se$ (101) plane has the intrinsic catalytic ability to generate/decompose $Li_2O_2$ during ORR/OER process, with better conductivity, lower overpotential and higher catalytic activity. As a consequence, $Co_{0.85}Se$@CNT-80 electrode exhibited remarkable cycle stability about 2448 h at 100 mA/g and 292 cycles at 500 mA/g, superior specific capacity of 9327.9 mAh/g.

The $Co_{0.85}Se$@CNT samples were fabricated by the one-step hydrothermal method following a heat treatment as shown in Fig. 1a. Samples were denoted as $Co_{0.85}Se$@CNT-80, $Co_{0.85}Se$@CNT-40, and pure $Co_{0.85}Se$, respectively, based on the addition of 80, 40, 0 mg of CNT in the synthesis process. The detailed morphologies of $Co_{0.85}Se$@CNT-80, $Co_{0.85}Se$@CNT-40, pure $Co_{0.85}Se$ nanoparticles and pure CNT captured by the field emission scanning electron microscope (SEM) were shown in Fig. 1b and Fig. S1 (Supporting information). The average diameter of pure CNT was about 30 nm with the length of several microns. After inlaying $Co_{0.85}Se$ nanocrystals, the surface of CNT became uneven with wrinkle-like protrusions. The pure $Co_{0.85}Se$ nanoparticles showed an irregular morphology with an average particle size of about 50 nm (Figs. S1b and c). Figs. 1c and d showed the transmission electron microscopy (TEM) and high-resolution transmission electron microscopy (HRTEM) images of $Co_{0.85}Se$@CNT-80. $Co_{0.85}Se$ nanocrystals were dispersedly embedded on the surface of CNT. The diffraction ring in the selected area electron diffraction (SAED) pattern of $Co_{0.85}Se$@CNT-80 (inset of Fig. 1c) could be perfectly indexed with the (101), (102) and (110) planes of $Co_{0.85}Se$ and the (100) plane of CNT, which further proved the formation of high crystalline $Co_{0.85}Se$@CNT composite. The high-resolution TEM (HRTEM) image in Fig. 1d showed the size of the $Co_{0.85}Se$ nanocrystals was 5–10 nm with the lattice *d*-spacing of 0.27 nm matched well with the (101) plane of $Co_{0.85}Se$, indicating the highly exposed (101)

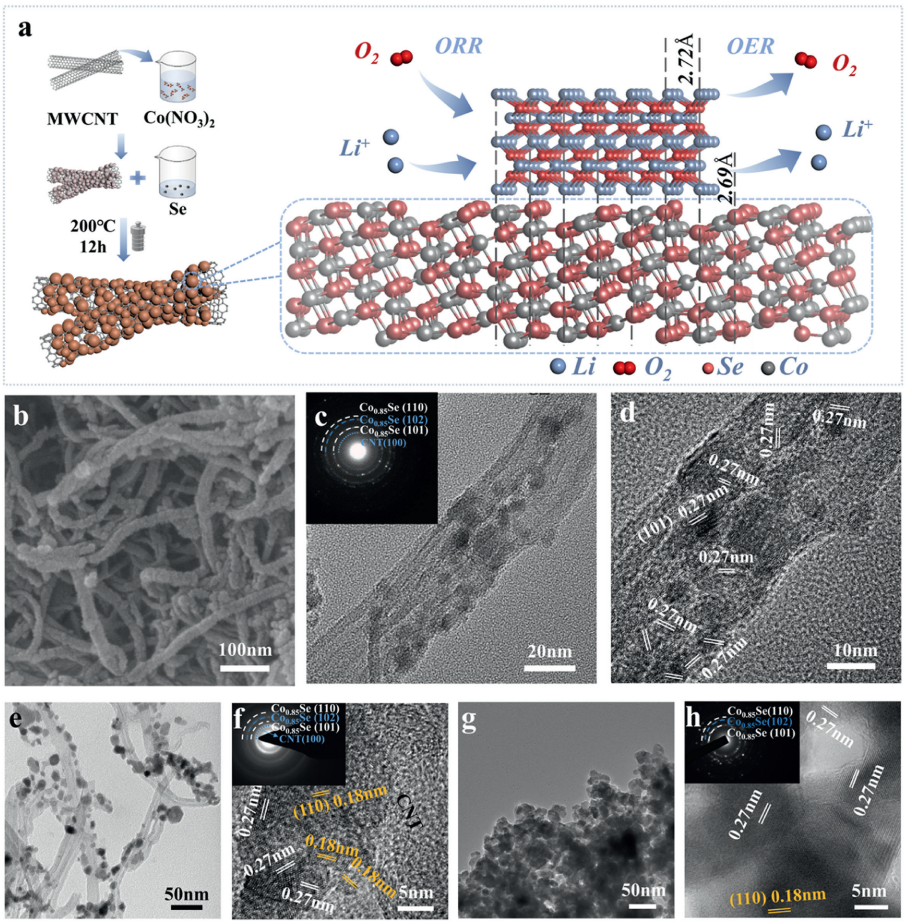


**Fig. 1.** (a) Schematic illustration of the synthetic process of $Co_{0.85}Se$@CNT and the ORR/OER at $Co_{0.85}Se$ (101) plane. (b) SEM, (c) TEM and (d) HRTEM images with SAED pattern of $Co_{0.85}Se$@CNT-80. (e) TEM and (f) HRTEM images with SAED pattern of $Co_{0.85}Se$@CNT-40. (g) TEM and (h) HRTEM images with SAED pattern of pure $Co_{0.85}Se$.

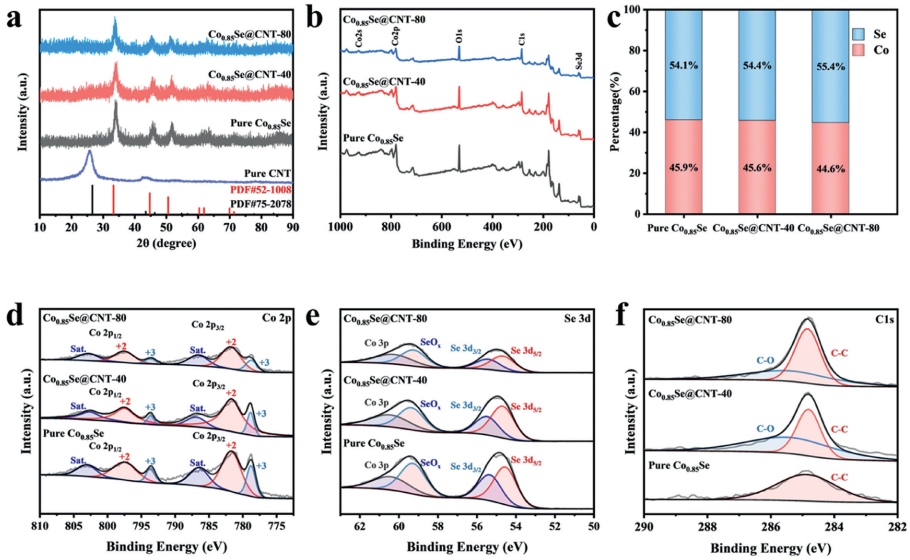


**Fig. 2.** (a) XRD patterns of $Co_{0.85}Se$@CNT and pure CNT. (b) XPS survey spectra, (c) Co:Se ratio and high-resolution of (d) Co 2p, (e) Se 3d, and (f) C 1s XPS spectra of $Co_{0.85}Se$@CNT.

plane for $Co_{0.85}Se$@CNT-80 sample. Figs. 1e–h showed the TEM and HRTEM images of $Co_{0.85}Se$@CNT-40 and pure $Co_{0.85}Se$ samples. The $Co_{0.85}Se$ particles on $Co_{0.85}Se$@CNT-40 exhibited a large particle size of about 20 nm and irregular morphology, which might be caused by the low content of CNT that decreased the surface area for the nucleation of $Co_{0.85}Se$ during synthesis process. The interlayer spacing of 0.18 nm and 0.27 nm corresponding to (110) plane and (101) plane of $Co_{0.85}Se$ were identified indicating the inhomogenous exposed crystal planes.

The $Co_{0.85}Se$ (101) plane has a surface spacing (2.69 Å) that closely matches with $Li_2O_2$ (100) plane (2.72 Å) with a mismatch degree smaller than 5%, which can act as a grain-refined agent to facilitate the nucleation and growth of peroxide on this plane (Fig. 1a), and in turn enhance the electrochemical performance of $Co_{0.85}Se$ cathode catalyst in LOBs. The lattice matching (101) plane can obtain superior adsorption capability for $Li_2O_2$ and $Li_4O_4$, optimized electronic state and catalytic capability for the formation/decomposition of $Li_2O_2$ (detail description see the following DFT calculation part).

X-ray diffraction (XRD) patterns of $Co_{0.85}Se$@CNT samples exhibited six diffraction peaks at 33.3°, 44.7°, 50.6°, 60.4°, 61.9° and 69.9°, corresponding to (101), (102), (110), (103), (112) and (202) planes of the hexagonal $Co_{0.85}Se$ (JCPDS No. 52–1008), respectively (Fig. 2a). The diffraction peak at 26.6° in pure CNT was matched to the (100) plane of CNT (JCPDS No. 75–2078). Therefore, the absence of secondary phase and other impurities confirmed the pure phase and high crystalline degree of the $Co_{0.85}Se$@CNT samples.

Fig. S2 (Supporting information) showed the $N_2$ adsorption/desorption isotherms of the four samples. The specific surface area of the four samples calculated by the BET (Brunauer-Emmett-Teller) method was 45.132 (pure $Co_{0.85}Se$), 66.561 ($Co_{0.85}Se$@CNT-40), 62.243 ($Co_{0.85}Se$@CNT-80), and 145.116 $m^2/g$ (CNT). The specific surface area of $Co_{0.85}Se$@CNT-80 was smaller than that of CNT probably due to the incorporation of $Co_{0.85}Se$ particles and their dense coating. Nevertheless, the specific surface area of $Co_{0.85}Se$@CNT-80 is approximately 1.4 times higher than that of pure $Co_{0.85}Se$ nanoparticles. The large specific surface area is beneficial to increase the active site and promote the wettability of electrolyte, thus improving the battery performance.

X-ray photoelectron spectroscopy (XPS) was applied to identify the surface electronic state and chemical composition of $Co_{0.85}Se$@CNT composites. The survey spectrum in Fig. 2b confirmed the signals of the Co, Se and C elements, and their core energy level spectra were shown in Figs. 2d-f, respectively. In the Co 2p spectra, Co $2p_{1/2}$, Co $2p_{3/2}$ and two satellite peaks were deconvoluted by a Gaussian fitting method. These peaks fitted well with the two spin-orbit doublets characteristic of $Co^{2+}$ and $Co^{3+}$. The binding energies of $Co^{3+}$ $2p_{3/2}$ and $Co^{3+}$ $2p_{1/2}$ were 778.69 and 793.92 eV, respectively, which agreed well with the reported values [32]. The 781.56 and 797.42 eV peaks were attributed to $Co^{2+}$ and the peaks observed at 786.80 and 802.59 eV were fitted with shakeup satellite peaks of Co 2p. The results indicated that cobalt mainly exists on the surface as $Co^{2+}$ and the presence of $Co^{3+}$ may be due to the Co vacancy [32,33]. Spectrum in Fig. 2e exhibited the electron-binding energies of 54.66 and 55.46 eV, corresponding to Se $3d_{5/2}$ and Se $3d_{3/2}$, respectively. On account of the surface oxidation of Se, the peak appeared at 59.35 eV was assigned to $SeO_x$ and the peak at 60.42 eV was attributed to Co 3p [34]. As illustrated in Fig. 2f, the high-resolution C 1s spectrum had two fitting peaks at 284.8 and 285.3 eV corresponding to C-C and C-O bonds, respectively. The contents of Co and Se were shown in Fig. 2c. The Co:Se ratios calculated from XPS spectra were 0.82 for $Co_{0.85}Se$@CNT-80 and pure $Co_{0.85}Se$, and 0.85 for $Co_{0.85}Se$@CNT-40, which was close to the stoichiometry.

The electrochemical performance of $Co_{0.85}Se$@CNT as the cathode catalyst of LOBs was carried out using the 2032-type coin cells with lithium sheet as the counter electrode. Fig. 3a exhibited the cyclic voltammetry (CV) curves of the four samples ($Co_{0.85}Se$@CNT-80, $Co_{0.85}Se$@CNT-40, pure $Co_{0.85}Se$, and pure CNT) at a scanning speed of 0.15 mV/s over a voltage range of 2.35–4.35 V. During the cathodic scan, all four catalysts showed reduction peaks, corresponding to the ORR process related to the formation of discharge product $Li_2O_2$ ($2Li^+ + O_2 + 2e^- \rightarrow Li_2O_2$). $Co_{0.85}Se$@CNT-80 had more positive ORR peak at 2.54 V. Meanwhile, during the anodic sweep, the oxidation peak of $Co_{0.85}Se$@CNT-80 located at 3.88 V, lower than that of $Co_{0.85}Se$-40 (4.24 V) and pure $Co_{0.85}Se$, which is connected with the bulk decomposition process of the discharge product ($Li_2O_2 \rightarrow O_2 + 2Li^+ + 2e^-$) while only a weak peak was detected in pure CNT. In short, compared with other electrodes, much higher anodic peak current and large integration area were achieved for the $Co_{0.85}Se$@CNT-80 electrode, implying that more discharge products can be reversibly decomposed and thus

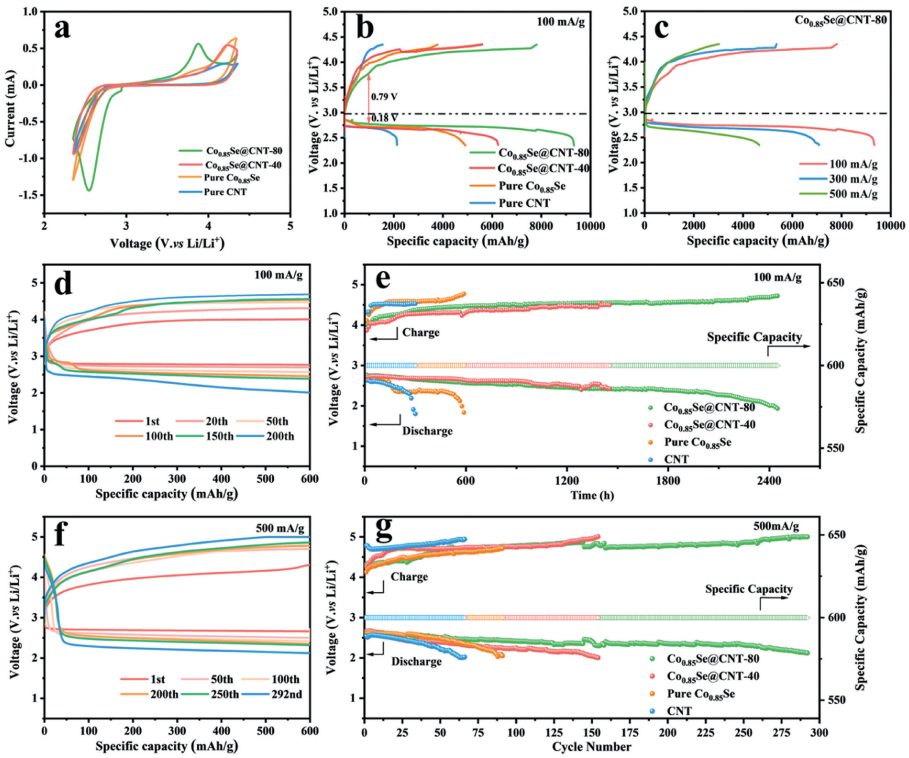


**Fig. 3.** (a) CV curves at a scan rate of 0.15 mV/s at a voltage window of 2.35–4.35 V. (b) Initial discharge/charge profiles at a current density of 100 mA/g over a voltage range of 2.35–4.35 V of different electrodes. (c) The discharge/charge profiles at various current densities ranging from 100 mA/g to 500 mA/g of $Co_{0.85}Se$@CNT-80. (d) The cycling performance of $Co_{0.85}Se$@CNT-80 and (f) terminal discharge-charge voltages of different electrodes at 100 mA/g with a limited capacity of 600 mAh/g. (e) The cycling performance of $Co_{0.85}Se$@CNT-80 and (f) terminal discharge-charge voltages of different electrodes at 500 mA/g with a limited capacity of 600 mAh/g.

much ameliorated catalytic kinetics performance. The electrochemical impedance spectroscopy (EIS) spectra of these four samples were also collected before and after the CV test under open-circuit voltage in the frequency range of $10^5$–0.01 Hz (Fig. S3 in Supporting information), and the charge transfer resistance ($R_{ct}$) can be evaluated by the semicircles diameter in the middle frequency range. The $Co_{0.85}Se$@CNT-80 electrode exhibited a $R_{ct}$ of 22.1 Ω before the CV test, which was lower than that of $Co_{0.85}Se$@CNT-40 (74.8 Ω), pure $Co_{0.85}Se$ (41.5 Ω) and CNT (51.7 Ω). After the CV test, the charge transfer resistance of these four samples all showed a tendency to increase. Notably, the $R_{ct}$ of $Co_{0.85}Se$@CNT-80 electrode (60.8 Ω) was also smaller than that of $Co_{0.85}Se$@CNT-40 (81.7 Ω), pure $Co_{0.85}Se$ (61.1 Ω) and CNT (82.1 Ω) after the CV test. The low $R_{ct}$ observed in the $Co_{0.85}Se$@CNT-80 electrode suggests a high efficiency of electron and ion transfer during ORR/OER. This characteristic facilitates the formation/decomposition of discharge products and contributes to an extended electrode lifespan.

The initial galvanostatic discharge-charge curves of four different cathodes were shown in Fig. 3b. It was noted that the $Co_{0.85}Se$@CNT-80 cathode delivered a specific capacity of 9327.9 mAh/g at a current density of 100 mA/g when discharged to 2.35 V. However, $Co_{0.85}Se$@CNT-40, pure $Co_{0.85}Se$, and pure CNT cathodes could only exhibit 6264.6, 4911.0 and 2132.4 mAh/g, respectively. Furthermore, the LOBs with $Co_{0.85}Se$@CNT-80 cathode could deliver a specific capacity of 7813.1 mAh/g when recharged to 4.35 V, which was much larger than that using $Co_{0.85}Se$@CNT-40, pure $Co_{0.85}Se$ and pure CNT cathodes (5621.4, 3780.3 and 1550.9 mAh/g). More importantly, the initial overpotentials for ORR/OER process of the $Co_{0.85}Se$@CNT-80 cathode were only 0.18/0.79 V with the voltage platforms of 2.73/4.19 V, which were remarkably lower than other cathodes, suggesting its superior electrocatalytic efficiency. The rate capability of the $Co_{0.85}Se$@CNT-80 cathode was checked at different current densities from 100 mA/g to 500 mA/g (Fig. 3c). The initial discharge/charge capacity at current densities of 100, 300 and 500 mA/g were 9327.9/7813.1, 7081.8/5360.4 and 4655.3/3023.1 mAh/g, respectively. As the current density increased, the specific capacity did not fade quickly. The durability of the catalytic ability of $Co_{0.85}Se$@CNT cathode in LOBs was evaluated by limiting the specific capacity at low and high current densities. Figs. 3d and e showed the selected discharge/charge profiles and terminal voltage of $Co_{0.85}Se$@CNT-80, $Co_{0.85}Se$@CNT-40, pure $Co_{0.85}Se$, and pure CNT cathodes at a current density of 100 mA/g and limited capacity of 600 mAh/g. The (101) plane highly exposed $Co_{0.85}Se$@CNT-80 cathode stably worked over 2400 h which was about 1.7 times longer than that of $Co_{0.85}Se$@CNT-40 cathode embedded by irregular $Co_{0.85}Se$ particles. On the contrary, the batteries with pure $Co_{0.85}Se$ and pure CNT cathodes died after 600 and 288 h, respectively. It is worth noting that the $Co_{0.85}Se$@CNT-80 cathode exhibited obviously lower ORR/OER overpotentials compared to other cathodes, in which the terminal discharge voltage was stable at around 2.62 V and the charge voltage stabilized at 4.36 V, indicating that the (101) plane highly exposed $Co_{0.85}Se$@CNT-80 cathode can efficiently and sustainably maintain its catalytic ability for the formation and decomposition of discharge product $Li_2O_2$. When the current density increased to 500 mA/g (Figs. 3f and g), the $Co_{0.85}Se$@CNT-80 electrode worked for 294 cycles with lower overpotentials compared to that of $Co_{0.85}Se$@CNT-40 electrode (154 cycles), suggesting that the superior reversibility of $Co_{0.85}Se$@CNT-80 cathode. For pure $Co_{0.85}Se$ and pure CNT, the voltage soon dropped to 2.0 V in the 91$^{st}$, and 63$^{rd}$ cycle revealed in Fig. 3g and Figs. S5-S7 (Supporting information). These results demonstrated that $Co_{0.85}Se$ catalyst with highly exposed (101) plane exhibited superior cycle stability, large specific capacity and low overpotentials. It is thought that the (101) plane with the lattice matching effect with $Li_2O_2$ contributed significantly to the performance improvement.

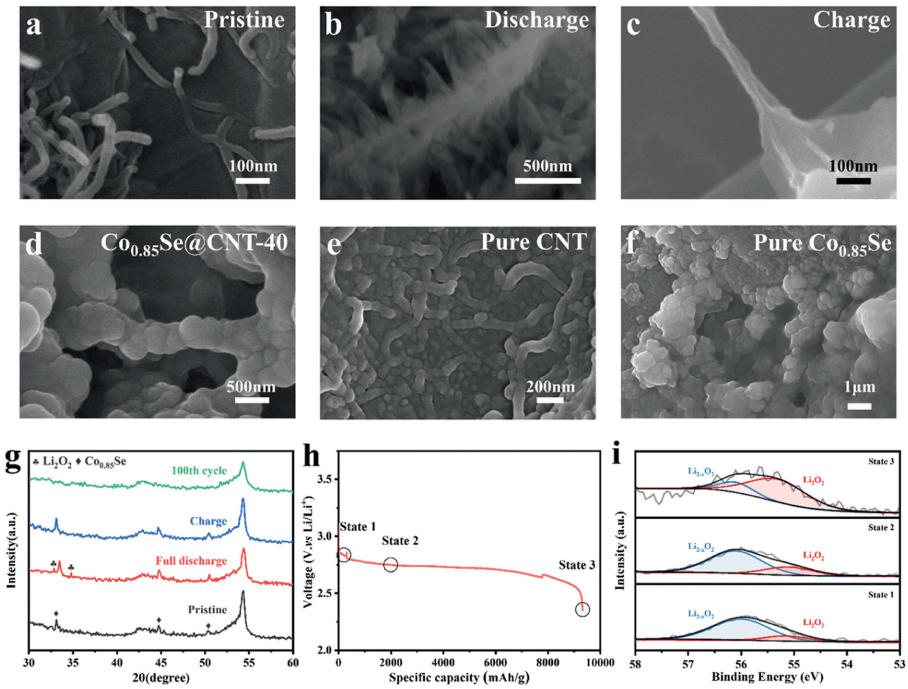


**Fig. 4.** SEM images of $Co_{0.85}Se$@CNT-80 electrode at (a) pristine, (b) full discharge, and (c) 1st recharged at the current density of 100 mA/g. SEM images of (d) $Co_{0.85}Se$@CNT-40, (e) pure CNT, and (f) pure $Co_{0.85}Se$ electrode at full discharge. (g) XRD patterns at different discharge/charge stages. (i) High-resolution XPS spectra of Li 1s at three selected states, corresponding to states (1–3) in (h), respectively.

To further investigate the underlying mechanism of the above-mentioned electrochemical performance improvements, the microstructures of discharged products and recharged electrodes during cycling were verified by *ex-situ* SEM, XRD spectroscopy, and XPS spectra, showing effective indicator of monitoring the oxygen reduction and evolution behaviors in LOBs. Figs. 4a-c showed the SEM images of pristine, full discharge, and recharged $Co_{0.85}Se$@CNT-80 electrode. At the pristine state, $Co_{0.85}Se$@CNT-80 presented a tubular structure with a diameter of about 30 nm, which was consistent with the previous characterization. After full discharge, the dendrite discharge products were observed with a size of 300 nm on the $Co_{0.85}Se$@CNT-80. After charging, the discharge products decomposed completely and the nanotube structure was restored. These results indicated the polarized nucleation and growth of the discharge products on $Co_{0.85}Se$@CNT-80 electrode, which would facilitate the infiltration of electrolyte, maintain the activity of tri-phase interface and accelerate the formation/decomposition kinetics of discharge products. It is deduced that the highly (101) plane is beneficial for the nucleation and growth of $Li_2O_2$. Figs. 4d-f showed the SEM images of $Co_{0.85}Se$@CNT-40, pure CNT and pure $Co_{0.85}Se$ electrodes after full discharge. It can be seen that $Co_{0.85}Se$@CNT-40 and CNT were still tubular structure after loading the products. The diameter of $Co_{0.85}Se$@CNT-40 tube increased to about 400 nm, and the diameter of CNT increased to 100 nm, which indicated that the formation of film-like discharge products. Similarly, the film-like products can be still seen on pure $Co_{0.85}Se$ particles (Fig. 4f).

Accordingly, as shown in *ex-situ* XRD pattern (Fig. 4g and Fig. S8 in Supporting information) of $Co_{0.85}Se$@CNT-80, there were two characteristic peaks except for the peaks of carbon paper and $Co_{0.85}Se$ after discharge, which belonged to $Li_2O_2$ [20]. The peaks disappeared after 1st, 10th, and 100th recharging, demonstrating the good reversible cycling performance of $Co_{0.85}Se$@CNT-80. Fig. 4i showed the *ex-situ* high-resolution XPS of Li 1s of $Co_{0.85}Se$@CNT-80 electrode in different discharge states (corresponding to Fig. 4h) at a current density of 100 mA/g to identify the evolution of the chemical state of discharge products. At the initial discharge (100 mAh/g), $Li_{2-x}O_2$ (a mixture of $LiO_2$ and $Li_2O_2$) with binding energies of about 56.10 eV [35–38] was the main discharge product. When discharged to 2000 mAh/g, the peak of $Li_2O_2$ with binding energies of about 55.07 eV [35,39] became stronger indicating the conversion from $Li_{2-x}O_2$ to $Li_2O_2$. After full discharge, $Li_2O_2$ became the dominant phase of the discharge products indicating the high-efficiency conversation from the intermediate to the final discharge products of the (101) plane highly exposed $Co_{0.85}Se$ cathode catalyst. For comparison, there was no obvious diffraction peaks of $Li_2O_2$ for the discharge product in the XRD pattern (Fig. S9 in Supporting information) of CNT electrodes after full discharge. The XPS spectra (Fig. S10 in Supporting information) showed that the products were mainly $Li_{2-x}O_2$ and a small amount of $Li_2CO_3$ and $Li_2O_2$. The existence of carbonate indicated that CNT was involved in the discharge reaction.

The polarized growth and composition evolution of discharge product demonstrated that the nucleation and growth of discharge products occurred directly on the surface of $Co_{0.85}Se$@CNT-80, in which the (101) plane of $Co_{0.85}Se$ played an important role in promoting the formation, conversation and growth of $Li_2O_2$. The highly exposed $Co_{0.85}Se$ (101) plane matches well with $Li_2O_2$ (100) plane and exhibits superior catalytic capability, which can act as a grain refiner, promoting the formation of a dendrite-like $Li_2O_2$ structure instead of a closed membrane.

To further demonstrate the superior catalytic capability of lattice matching plane and the mechanism during ORR/OER process of the $Co_{0.85}Se$ catalyst, DFT calculations are conducted to provide reaction information at atomic scale. The (101) and (110) planes detected by HRTEM were selected for calculations. Fig. 5a shows the electron localization function (ELF) diagrams of (101) and (110) planes. The function ranges from 0 to 1, where values of 0, 0.5, and 1 represent very low charge density, completely delocalized electrons, and completely localized electrons, respectively [40–42]. It can be seen that the electrons are mainly concentrated on Se atom, while the charge density around Co is extremely low. The blue area

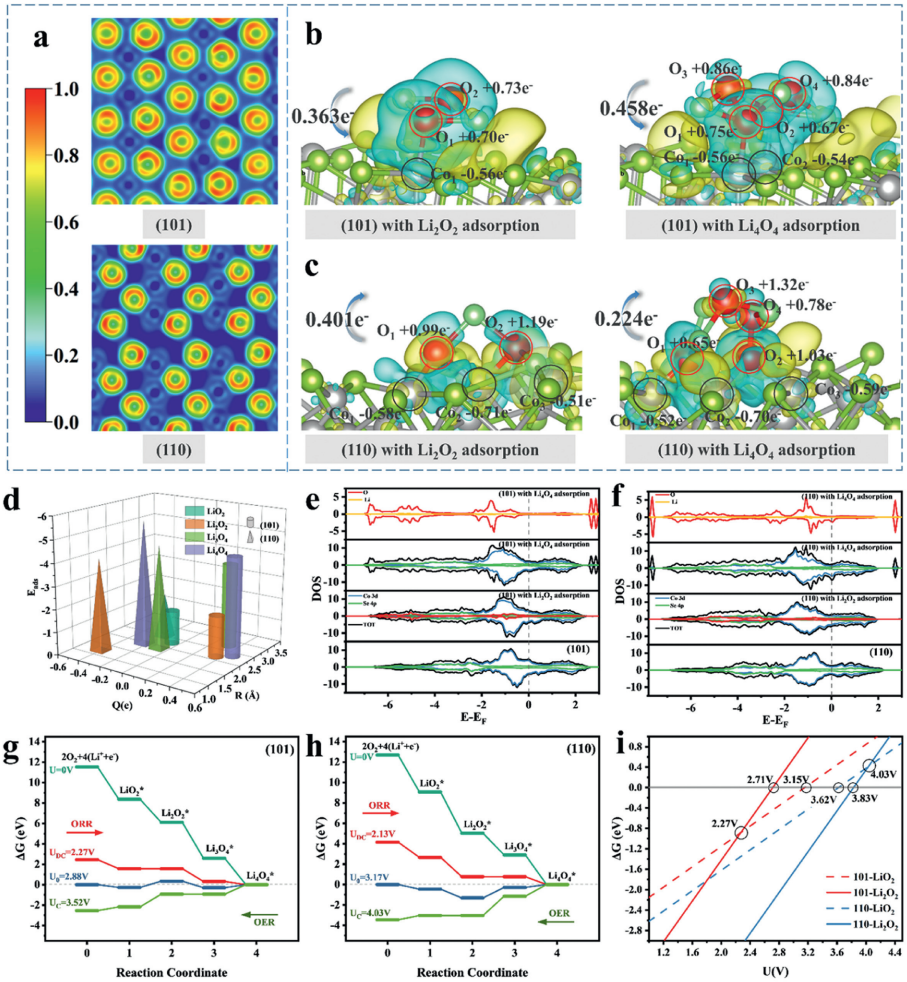


**Fig. 5.** (a) Electron localization function (ELF) diagrams of (101) plane and (110) plane. Charge density difference plots of $Li_2O_2^*$ and $Li_4O_4^*$ on (b) (101) plane and (c) (110) plane. (d) Bader charge transfer (Q), adsorption energy ($E_{ads}$), and distance (Å) between different adsorbates and substrates on $Co_{0.85}Se$ (101) and (110) planes. DOS map before and after binding of $Li_2O_2$ and $Li_4O_4$ for the $Co_{0.85}Se$ (e) (101) plane and (f) (110) plane. Calculated energy diagram of $Co_{0.85}Se$ (g) (101) plane and (h) (110) plane in the ORR and OER processes. (i) Phase diagrams of the cathode reaction on $Co_{0.85}Se$ (101) and (110) planes.

in the (110) plane is deeper, which means that the stronger polarization of the Co-Se bond on the (110) plane. Compared with (110) plane, the green area (where electrons are fully delocalized) of (101) plane is arranged more closely and uniformly, which is conducive to the efficient transfer of electrons during the catalytic reaction process. Figs. 5b and c show the charge density difference diagrams and Bader charge of bonded Co and O atoms of (101) and (110) planes adsorbed with $Li_2O_2$ and $Li_4O_4$. An evident charge transfer can be observed between the adsorbents and the substrate (yellow and blue represent the increase and decrease in charge density, respectively). On both planes, charge transfer paths are established between the substrate and the adsorbents *via* Co–O bonds, with Co acting as charge transfer center. The difference is that the adsorption site of O atom on (101) plane is the Co top site, while on (110) plane is the Co-Co bridge bond. Additionally, one oxygen atom of $Li_2O_2$ after adsorption on (110) plane is almost detached and bonded to the Co atom on the surface (Fig. 5c), which could lead to instability of the peroxide on the surface and be detrimental to the OER process. On the contrary, the structure of $Li_2O_2$ on (101) plane remains basically unchanged. Compared to the (101) plane, the O atoms on (110) plane acquire more charge and form stronger Co-O bonds after the adsorption of $Li_2O_2$ and $Li_4O_4$. Fig. 5d and Table S1 (Supporting information) depict the Bader charge transfer ($Q$), adsorption energy ($E_{ads}$), and distance (Å) between the different adsorbents and substrates on the (101) and (110) planes. It can be seen that the (101) plane shows low adsorption energy and considerable distance between the adsorbent and the substrate, which is conducive to the ORR/OER reaction. Especially for $Li_2O_2$, the adsorption energy on the (110) plane (−4.08 eV) significantly exceeds that on the (101) plane (−1.85 eV). The large adsorption energy may be attributed to the large change in the $Li_2O_2$ structure on the (110) plane. In addition, the Bader charge of (110) plane adsorbed $Li_2O_2$ is negative while that of (101) is positive. The negative Bader charge of (110) plane signifies a greater charge exchange between O atoms of $Li_2O_2$ and Co atoms on (110) plane, indicating stronger Co-O bonds. This is consistent with the large adsorption energy. Large adsorption energy and increased charge exchange will hinder the decomposition of $Li_2O_2$ during the OER reaction.

Furthermore, the electron density of state (DOS) diagram of $Co_{0.85}Se$ (101) and (110) plane before and after adsorption of $Li_2O_2$ and $Li_4O_4$ obtained by DFT calculations are shown in Figs. 5e and f. The electronic state distributions near the Fermi energy level exist in both planes, where the DOS value of the (101) plane is larger than that of the (110) plane, indicating the excellent conductivity and charge transfer efficiency of the former. After loading $Li_2O_2$ and $Li_4O_4$, the total DOS of (101) plane near the Fermi level decreases slightly because of the poor conductivity of the adsorbents. In addition, the obvious overlap between the O and Co 3d orbitals observed in the DOS signifies their interaction, which provides ev-

idence for the existence of Co-O bond. For (110) plane, the total DOS near the Fermi level increases slightly after loading $Li_2O_2$. After loading $Li_4O_4$, the total DOS increases significantly and the O and Co 3d orbitals contributed to the increase, which is consistent with the previously mentioned strong Co-O binding on (110) plane. It is unfavorable for the desorption of reaction products during OER process. The instability of the Co electronic structure is detrimental to the maintenance of catalyst stability. In contrast, stable DOS of (101) plane indicates the excellent charge transfer ability and bifunctional catalytic capability for LOBs.

Figs. 5g and h record the calculated energy diagrams for ORR and OER procedures on the (101) and (110) plane. Four elementary reaction steps for the generation of $Li_4O_4$ are considered as following: (I) $(Li^+ + e^-) + O_2 \leftrightarrow LiO_2^*$, (II) $LiO_2 + (Li^+ + e^-) \leftrightarrow Li_2O_2^*$, (III) $Li_2O_2 + (Li^+ + e^-) + O_2 \leftrightarrow Li_3O_4^*$, and (IV) $Li_3O_4 + (Li^+ + e^-) \leftrightarrow Li_4O_4^*$. Where the symbol * indicates that the species are adsorbed on the surface. Compared with (110) plane ($\eta_{ORR}/\eta_{OER} = 1.04/0.86$ V; $\eta_{TOT} = 1.90$ V), (101) plane exhibits lower overpotentials ($\eta_{ORR}/\eta_{OER} = 0.61/0.64$ V; $\eta_{TOT} = 1.25$ V) during discharge/charge processes. Fig. 5i depicts the reaction phase diagram for the generation of $LiO_2$ and $Li_2O_2$ on (101) and (110) planes. On (101) plane, $LiO_2$ is spontaneously formed initially when the discharge voltage is between 2.27 V and 3.15 V due to lower $\Delta G$ of $LiO_2$. Meanwhile, $Li_2O_2$ also formed when the discharge voltage is lower than 2.71 V and the conversion from $LiO_2$ to $Li_2O_2$ occurs at 2.27 V. The result is consistent with *ex-situ* XPS that the initial product of the (101) plane highly exposed $Co_{0.85}Se$@CNT-80 is $LiO_2$. For (110) plane, $Li_2O_2$ is preferentially generated below 3.82 V, while $LiO_2$ is also produced below 3.62 V, so the product on (110) is mainly $Li_2O_2$ and $LiO_2$, which is consistent with the observation of the *ex-situ* XPS on the pure $Co_{0.85}Se$ electrode (Fig. S9 in Supporting information). DFT calculations reveal that the lattice matching (101) plane of $Co_{0.85}Se$ exhibits excellent bifunctional catalytic performance with uniform electron distribution, efficient charge transfer, and lower overpotentials. The (101) plane acts as a grain refiner and forms dendritic $Li_2O_2$ instead of membranous $Li_2O_2$ by a single-electron reaction.

In conclusion, $Co_{0.85}Se$@CNT catalysts with a well-designed structure were successfully prepared by a simple one-pot hydrothermal method and used as a cathode catalyst for lithium-oxygen batteries. $Co_{0.85}Se$ can effectively reduce the overpotential due to its intrinsic metal conductivity and the lattice matching effect with $Li_2O_2$. The $Co_{0.85}Se$@CNT-80 electrodes exhibited superior cycle stability, cycling over 2448 h at 100 mA/g and lower discharge/charge overpotentials due to smaller particle size and large exposed lattice matching (101) plane, which serves as a template for growth of $Li_2O_2$ and promotes epitaxial growth of $Li_2O_2$. The *ex-situ* analysis showed that crystalline $Li_2O_2$ accumulated as dendrites on the $Co_{0.85}Se$@CNT-80 under the assistant of $Co_{0.85}Se$ without other by-products. DFT calculations revealed that the Co acts as the adsorption site and charge transfer center, and the lattice matching (101) plane exhibits excellent catalytic ability for ORR and OER due to its homogeneous electron distribution, suitable adsorption energy and promoted $Li_2O_2$ growth kinetics. The present work not only demonstrates the electrocatalytic performance of $Co_{0.85}Se$@CNT, but also expands the selection and design of efficient catalysts by lattice matching.

## Acknowledgments

This work was supported by National Natural Science Foundation of China (Nos. 52173286, 52207249), Major basic research project of Natural Science Foundation of Shandong Province (No. ZR2023ZD12), the State Key Laboratory of Marine Resource Utilization in South China Sea (Hainan University) (No. MRUKF2023013) and Open Program of Guangxi Key Laboratory of Information Materials (No. 221024-K).

## Supplementary materials

Supplementary material associated with this article can be found, in the online version, at doi:10.1016/j.cclet.2024.109595.

## References

[1] M. Armand, J.M. Tarascon, Nature 451 (2008) 652–657.
[2] D. Aurbach, B.D. McCloskey, L.F. Nazar, P.G. Bruce, Nat. Energy 1 (2016) 16128.
[3] P.G. Bruce, S.A. Freunberger, L.J. Hardwick, J.M. Tarascon, Nat. Mater. 11 (2012) 19–29.
[4] Q. Xiong, G. Huang, X.B. Zhang, Angew. Chem. Int. Ed. 59 (2020) 19311–19319.
[5] T. Ogasawara, A. Débart, M. Holzapfel, P. Novak, P.G. Bruce, J. Am. Chem. Soc. 128 (2006) 1390–1393.
[6] L. Grande, E. Paillard, J. Hassoun, et al., Adv. Mater. 27 (2015) 784–800.
[7] W.J. Kwak, D.Sharon Rosy, et al., Chem. Rev. 120 (2020) 6626–6683.
[8] F.J. Li, J. Chen, Adv. Energy Mater. 7 (2017) 1602934.
[9] C.Z. Shu, J.Z. Wang, J.P. Long, H.K. Liu, S.X. Dou, Adv. Mater. 31 (2019) 1804587.
[10] J.M. Tarascon, M. Armand, Nature 414 (2001) 359–367.
[11] C. Xia, C.Y. Kwok, L.F. Nazar, Science 361 (2018) 777–781.
[12] G.L. Zhang, C.Y. Liu, L. Guo, et al., Adv. Energy Mater. 12 (2022) 2200791.
[13] J. Xie, X.H. Yao, Q.M. Cheng, et al., Angew. Chem. Int. Ed. 54 (2015) 4299–4303.
[14] F.J. Li, T. Zhang, H.S. Zhou, Energy Environ. Sci. 6 (2013) 1125–1141.
[15] M.D. Bhatt, H. Geaney, M. Nolan, C. O'Dwyer, Phys. Chem. Chem. Phys. 16 (2014) 12093–12130.
[16] Y. Dou, Z. Xie, Y. Wei, Z. Peng, Z. Zhou, Natl. Sci. Rev. 9 (2022) nwac040.
[17] S.M. Zhang, M.H. Chen, X. Zhao, et al., Electrochem. Energy Rev. 4 (2021) 336–381.
[18] F.Y. Cheng, J. Chen, Chem. Soc. Rev. 41 (2012) 2172–2192.
[19] Y.Y. Shao, F. Ding, J. Xiao, et al., Adv. Funct. Mater. 23 (2013) 987–1004.
[20] B. He, G. Li, J. Li, et al., Adv. Energy Mater. (2021) 2003263.
[21] L. Johnson, C.M. Li, Z. Liu, et al., Nat. Chem. 6 (2014) 1091–1099.
[22] X. Liu, X. Song, Q. Zhang, et al., J. Energy Chem. 69 (2022) 516–523.
[23] B.M. Gallant, R.R. Mitchell, D.G. Kwabi, et al., J. Phys. Chem. C 116 (2012) 20800–20805.
[24] M.M.O. Thotiyl, S.A. Freunberger, Z.Q. Peng, P.G. Bruce, J. Am. Chem. Soc. 135 (2013) 494–500.
[25] M. Balaish, A. Kraytsberg, Y. Ein-Eli, Phys. Chem. Chem. Phys. 16 (2014) 2801–2822.
[26] H.G. Jung, J. Hassoun, J.B. Park, Y.K. Sun, B. Scrosati, Nat. Chem. 4 (2012) 579–585.
[27] Y. Wang, J. Wang, Z. Mohamed, et al., Appl. Mater. Today 19 (2020) 100603.
[28] Z.L. Li, S. Ganapathy, Y.L. Xu, et al., Adv. Energy Mater. 8 (2018) 1703513.
[29] J. Lu, L. Cheng, K.C. Lau, et al., Nat. Commun. 5 (2014) 4895.
[30] S.T. Plunkett, A. Kondori, D.Y. Chung, et al., ACS Energy Lett. 7 (2022) 2619–2626.
[31] Z.C. Wu, J.J. Li, Z.X. Zou, X. Wang, J. Solid State Electrochem. 22 (2018) 1785–1794.
[32] Y.X. Huang, Z.H. Wang, Y. Jiang, et al., Nano Energy 53 (2018) 524–535.
[33] S.J. Shen, Z.P. Lin, K. Song, et al., Angew. Chem. Int. Ed. 60 (2021) 12360–12365.
[34] Y. Han, X. Chen, C. Qian, et al., Chem. Eng. J. 420 (2021) 130461.
[35] H. Zhou, L. Guo, R. Zhang, et al., Adv. Funct. Mater. (2023) 2304154.
[36] R. Liu, Y. Fu, G. Zhang, et al., J. Mater. Chem. A 10 (2022) 18078–18086.
[37] D. Li, L. Zhao, Q. Xia, et al., Adv. Funct. Mater. 32 (2022) 2108153.
[38] G. Li, N. Li, S. Peng, et al., Adv. Energy Mater. 11 (2021) 2002721.
[39] L. Guo, L. Tan, A. Xu, et al., Energy Storage Mater. 50 (2022) 96–104.
[40] H. Huang, C. Cheng, G. Zhang, et al., Adv. Funct. Mater. 32 (2022) 2111546.
[41] G. Zhang, G. Li, J. Wang, et al., Adv. Energy Mater. 12 (2022) 2103910.
[42] A.D. Becke, K.E. Edgecombe, J. Chem. Phys. 92 (1990) 5397–5403.